Photoacoustics 40 (2024) 100644

Contents lists available at ScienceDirect

Photoacoustics

journal homepage: www.elsevier.com/locate/pacs

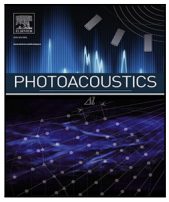

Dual-tube MEMS-based spectrophone for sub-ppb mid-IR photoacoustic gas detection

Stefano Dello Russo [a,b,1], Jacopo Pelini [b,c,1], Inaki Lopez Garcia [b], Maria Concetta Canino [d], Alberto Roncaglia [d], Pablo Cancio Pastor [b], Iacopo Galli [b], Paolo De Natale [b], Simone Borri [b,2,*], Mario Siciliani de Cumis [a,b,**,2]

[a] ASI Agenzia Spaziale Italiana - Centro di Geodesia Spaziale, Località Terlecchia, Matera, 75100, Italy
[b] CNR-INO - Istituto Nazionale di Ottica, and LENS, via N. Carrara 1, Sesto Fiorentino, 50019, Italy
[c] University "Federico II", Corso Umberto I 40, Naples, 80138, Italy
[d] Istituto per la Microelettronica e Microsistemi (IMM) Consiglio Nazionale delle Ricerche (CNR), Via P. Gobetti 101, Bologna, 40129, Italy

ARTICLE INFO

Keywords:
Trace-gas sensor
Photo-acoustic spectroscopy
Dual tube configuration
Acoustic enhancement
Minimum detection limit
Micro-electro-mechanical system (MEMS)
Sub-part-per-billion

ABSTRACT

Nowadays, the scientific community and industry are increasingly pressed to provide solutions for developing compact and highly-performing trace-gas sensors for several applications of crucial importance, such as environmental monitoring or medical diagnostics. In this context, this work describes a novel configuration, making use of a mid-IR spectrophone combining the compactness of a photo-acoustic setup, a non-conventional micro-electro-mechanical (MEMS) acousto-to-voltage transducer, and the sensitivity enhancement given by a cost-effective and easy-to-build dual-tube resonator configuration. In the optimal condition of sample pressure, the system developed in this work can achieve a minimum detection limit (MDL) equal to 0.34 ppb when averaging up to 10 s. Compared with previous literature of single-pass photoacoustic-based sensors for N_2O, this corresponds to a significant improvement both for the achieved normalized noise equivalent absorption coefficient (NNEA) equal to 1.41×10^{-9} $cm^{-1}WHz^{-1/2}$, and for a Noise-Equivalent-Concentration (NEC) of 1 ppb obtained at 1 s of averaging time.

1. Introduction

The mid-infrared is the region of the electromagnetic spectrum *par excellence* for gas sensing [1–4]. Thanks to the strong, fundamental molecular ro-vibrational transitions, high selectivity and sensitivity can be simultaneously obtained. For this reason, the development of increasingly high-performance sensors is a hot research topic: sampling very low quantities of substance, sensing a large variety of gases, covering wide pressure ranges, and an overall cheap spectrometer are key parameters, addressed by set-ups in continuous evolution [5–7].

In this framework, pushing toward higher detection sensitivities when simultaneously miniaturizing the entire system, will enable the fabrication of more compact and high-performing sensors to be deployed for in-situ applications [8–10]. Among all the various direct absorption spectroscopic schemes, photoacoustic-based setups represent an interesting compromise between performance and size, demonstrating promising and significant improvements [11–16].

This technique lays on simple physical principles [17,18]: when the laser beam's wavelength is resonant with a molecular transition of the selected trace-gas, the latter will absorb the impinging energy, jumping to its associated excited state. If the de-excitation dynamics is non-radiative, the relaxation to the ground state will occur by transferring its kinetic energy to the surrounding molecules through collisions, resulting in the generation of a pressure wave, and local thermal expansion of the sample. If the excitation beam is modulated (in amplitude or frequency) this phenomenon will be periodic, resulting in the generation of sound waves. Finally, exploiting a sensitive acoustic-to-voltage transducer, the latter are converted into a measurable signal, known as the photo-acoustic signal, from which it is possible to give an estimation of the sensor's final detection sensitivity.

Alongside traditional photo-acoustic detection schemes, two alternative variations have emerged, demonstrating promising results: Quartz-Enhanced (QEPAS) and Cantilever-Enhanced (CEPAS) photo-acoustic spectroscopy. In the former, a small quartz tuning fork (QTF)

* Corresponding author.
** Corresponding author at: ASI Agenzia Spaziale Italiana - Centro di Geodesia Spaziale, Località Terlecchia, Matera, 75100, Italy.
E-mail addresses: simone.borri@ino.cnr.it (S. Borri), mario.sicilianidecumis@asi.it (M. Siciliani de Cumis).
[1] Stefano Dello Russo and Jacopo Pelini contributed equally to this work.
[2] Simone Borri and Mario Siciliani de Cumis equally contribute to this work.

https://doi.org/10.1016/j.pacs.2024.100644
Received 12 August 2024; Received in revised form 5 September 2024; Accepted 5 September 2024
Available online 12 September 2024

is exploited as a microphone [19,20], while in the latter this role is played by a silicon-based cantilever [21,22]. Even if the sound wave's transduction occurs via the sensitive element's oscillations in both cases, these approaches are extremely different regarding the microphone's acousto-mechanical properties and the readout method. In fact, for CEPAS-based instruments, the mechanical resonance frequencies range from hundreds of Hertz to a few kilo-Hertz [23,24], while in QEPAS-based setups the QTF typically works around 30 kHz [25,26], although recent studies report the realization and implementation of lower frequency QTFs, even below 10 kHz [27,28], optimized for QEPAS sensing. Furthermore, the QTFs oscillations are measured via an electronic readout taking advantage of the quartz's piezo-resistivity. While for silicon based-cantilever the readout is all-optic, typically via interferometric-based techniques, allowing the measurements of extremely small displacement, thus reaching high sensitivities. Nevertheless, operation at relatively low frequencies, below 1 kHz, where noise is generally dominated by the 1/f electronic flicker noise [29,30] and by the acoustic noise, can significantly reduce the signal-to-noise ratio.

For this reason, taking advantage of the immense possibilities offered by micro-electro-mechanical systems (MEMS), silicon-based passive mechanical structures have been designed and realized to be exploited as performing sensitive elements in a photo-acoustic setup [31], aiming at simultaneously achieving a significant elongation following the interaction with the generated acoustic wave, and efficient acoustic-to-voltage signal transduction via an all-optical interferometric readout [32], similarly to what happens in quantum optomechanical experiments [33].

In this framework, a novel photo-acoustic spectrophone has been developed in this work to be used for all-optical detection, as in CEPAS sensors. This approach combines the advantages of high performance, robustness of operation, and ease of construction. The main focus is the sound conversion optimization, leveraging first on sound amplification and then on acousto-to-optical transduction with new geometry. Indeed, although the interferometric-based reading system is, by definition, extremely sensitive, conveying the pressure wave onto a suitable geometry by using appropriate "sound amplification systems" paves the way to a significant increase in the photo-acoustic signal [34,35].

Based on these assumptions, a "racket-shaped" silicon-based MEMS, resonant at around 7 kHz and exploited as acoustic-to-voltage transducer, has been coupled with a dual-tube configuration for proper acoustic wave confinement and intensity amplification. The analysis has been developed in three parts. (1): four different dual-tube systems, characterized by a similar geometry (in length and internal diameter) have been realized. Two of them have been fabricated with plastic materials, commonly used in 3D printers and particularly easy to handle, while the other two are metallic tubes widely exploited in QEPAS sensors [36]. Each of them has been coupled with the transducer to quantify the signal enhancement compared to the "bare-MEMS" configuration (i.e. without any acoustic resonance). (2): Once having determined the best material, several dual-tube systems with different lengths and internal diameters have been tested to find out the best enhancement performance. (3): with the best couple of geometric parameters the spectrophone's detection sensitivity has been tested, at a fixed trace-gas concentration and varying the sample pressure within a range from 8 mbar to 335 mbar. Finally, both the long-term stability and the achievable minimum detection limit of the spectrophone have been analyzed at the best pressure working point (i.e. where the signal-to-noise ratio is the highest).

2. Spectrophone design and optimization

Photoacoustic detection, regardless of the detection system, occurs through the motion of a structure following its interaction with an impacting pressure wave. By modifying the geometries around the sensitive element it is possible to locally increase the amplitude of the impacting pressure wave, for the same number of target molecules involved, and consequently increase the spectrophone's sensitivity. In particular, the conventional symmetry used is cylindrical for laser-based PA techniques, developed in two possible variants. In the first case, the laser beam is accommodated between a single tube equipped with an aperture in correspondence with the sensitive element (single-tube configuration) [37–39], while in the second case the laser beam passes through a pair of millimetric tubes, defining the so-called dual-tube configuration [35,40]. The spectrophone developed in this work, and whose 3D sketch is depicted in Fig. 1**(b)**, takes its inspiration from the second configuration.

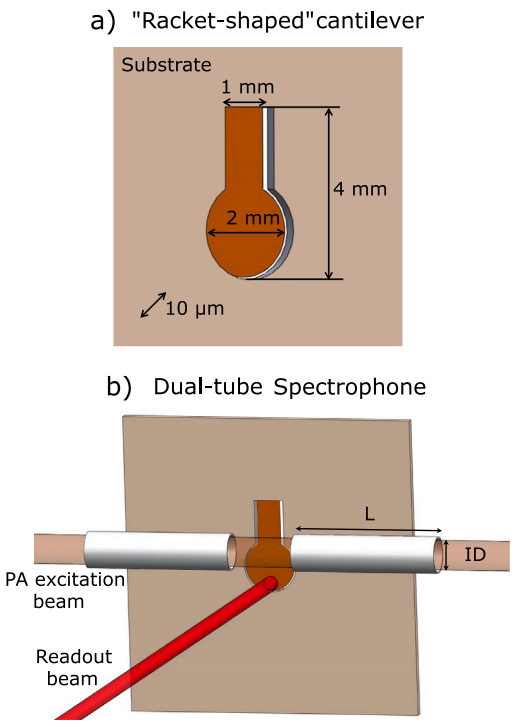

Fig. 1. **(a)**: front view of the "racket-shaped" cantilever and its associated dimensions. The oscillating structure is depicted in darker orange, while the substrate is colored in lighter orange. **(b)**: front view of the assembled spectrophone, made by the coupling of the MEMS with a dual-tube acoustic resonator system. The laser beam exploited for the photo-acoustic effect (PA excitation beam, depicted in light orange) is aligned to cross co-axially the tubes, thus maximally exploiting the acoustic wave intensity enhancement. The readout beam used to convert the structure's oscillation into a measurable voltage signal via an interferometric readout is colored in red and aligned with the region affected by the highest displacement.

The MEMS structure selected as the acoustic-to-voltage transducer is a "racket-shaped" cantilever similar to a conventional rectangular cantilever [41] but with a geometry optimized for efficient interaction with generated acoustic waves.

As shown in Fig. 1**(a)**, this structure has a lower base equal to 1 mm (corresponding to the only part in which the structure is anchored to its substrate), a total height of 4 mm, a free-end diameter of 2 mm, and a thickness of 10 µm. The resonance frequency has been preliminary evaluated via finite element modeling (FEM). An experimental investigation has been performed in Ref. [31], measuring a resonance frequency equal to 7.18 kHz at a pressure of 20 mbar, associated with a quality factor of approximately 1500.

Finally, a custom-made support has been realized to accommodate the resonator tubes as close as possible to the structure without touching it and to guarantee good collinearity with the excitation laser beam (colored in blurred orange in Fig. 1**(b)**). The device's free end, affected by the highest displacement following the interaction with the acoustic wave, is aligned with the readout probe beam (in red) to maximize the transduction efficiency.

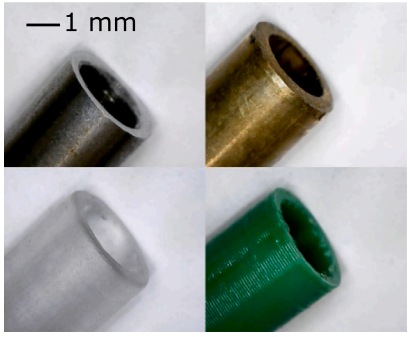

Fig. 2. Front-side view of the four different resonators under investigation: stainless steel (top left), brass (top right), UV resin (bottom left), and PLA (bottom right).

Table 1
Material, length (L), internal diameter (I_D), and external diameter (E_D) of the four different resonators investigated. The small discrepancies between internal diameters depend on the manufacturing process of each material.

Material	L (mm)	I_D (mm)	E_D (mm)
Stainless steel	19.20	2.75	3.98
Brass	19.20	2.75	4.00
PLA	19.20	2.75	3.99
UV resin	19.20	2.81	4.09

According to the theory, the optimal length of the resonators, L, is linked to the chosen MEMS resonance frequency, f, by the equation [35]:

$$L = \frac{v_s}{2f} - \frac{16 I_D}{3\pi} \quad (1)$$

where v_s is the speed of sound and I_D is the resonator internal diameter. The optimal length of an open-ended tube differs from a closed resonator by a factor of $8I_D/3\pi$ for each opening [42,43]. This difference, known as open-end correction (OEC), takes into account the boundary conditions existing for a standing wave of a specific frequency inside the resonator: compared to the case of closed resonators, the anti-nodes appear slightly outside the tubes due to the interaction between the resonator and the external environment, reducing its optimal length. Although for each I_D there is a unique correspondence with the optimal length, there is no analytical methodology that links the chosen pair (L, I_D) to the effective acoustic enhancement. For this reason, as a first approximation, the dimensions of the resonator's tube have been chosen taking inspiration from studies previously carried out with similar PA-based setups. In particular, in the work of Patimisco et al. [26], a pair of tubes with an internal diameter equal to 1.6 mm have been exploited for the amplification of a 12.46 kHz sound wave. By operating a simple proportion, an internal diameter of approximately 2.77 mm and consequently a length of 19.18 mm (according to Eq. (1)) represent good values for an efficient amplification of our 7.18 kHz sound wave frequency.

In addition to the size, the fabrication material could also play a fundamental role in the amplification capability of the dual-tube system. Hence, a comparative analysis of these two properties is crucial. Accordingly, four different types of material have been selected to quantify any differences in performance related to chemical-physical features or production defects. Two pairs have been made via 3D printing/additive manufacturing in UV curing resin and Polylactic acid (PLA) via liquid crystal display (LCD) resin printer and filament printer respectively. The other two, made of stainless steel and brass, have been fabricated with more common computerized numerical control (CNC) techniques and subtractive manufacturing.

Fig. 2 shows the front-side view of the four types of resonators realized for the comparison, while Table 1 reports the associated length, internal diameter, and external diameter (measured with a digital caliper with a precision of 0.01 mm). A more accentuated surface roughness, due to the limitations of the manufacturing technique, can be observed for PLA resonators (machine resolution 200 μm). The surface roughness of the resin tubes, although barely visible from the image, is slightly worse compared to one of the metal resonators, with a nominal machine resolution of 50 μm (pixel size of the LCD display). This characteristic of resonators made with additive manufacturing could compromise the optimal coupling conditions between resonators and MEMS.

As reported later in Section 4, a preliminary comparison has been made to choose the best resonator's fabrication material in terms of performance, costs, environmental impact, and production times. Once the material has been selected, a series of dual-tube resonators with different lengths and internal diameters have been realized to find out the geometric configuration associated with the highest acoustic enhancement. Finally, the sensitivity performances of the optimized spectrophone have been studied varying the sample pressure.

3. Experimental setup

A schematic representation of the setup developed for MEMS–resonator acoustic enhancement analysis is reported in Fig. 3. A mid-infrared continuous-wave (CW) Quantum Cascade Laser (QCL), is used for the acoustic wave generation addressing, with an impinging optical power of 15 mW, a well-isolated N_2O ro-vibrational transition at 2189.273 cm^{-1} and characterized by a line-strength equal to 2.14 × 10^{-19} cm/molecule. The QCL is managed in current and temperature, the latter set at 20 °C, via an integrated modular controller provided by ppq Sense S.R.L. (QubeCL 52) and through a waveform generator (WFG), used as an external current modulator, to scan the absorption feature via a low-frequency ramp (2 mHz). The emitted radiation is first conveyed into an optical isolator (OI, COHERENT FM2 MID-IR 4.55 μm), to avoid feedback, and subsequently into an acousto-optical modulator (AOM, M1208-G80-4), triggered by the WFG, for intensity modulation at the MEMS resonance frequency, thus allowing the acoustic wave generation following the trace-gas non-radiative relaxation. This approach is usually called 1-f amplitude modulation (1-f AM) [44]. The laser beam finally enters the gas chamber through a Zinc Selenide (ZnSe) wedged window, after being focused through a Calcium Fluoride (CaF_2) Plano-Convex Lens with a focal length of 150 mm. The beam diameter at the lens plane is 2 mm, resulting in a beam diameter of ~0.43 mm at the focal plane of the lens, also corresponding with the center of the MEMS. The ZnSe output window and the power meter (PM) in Fig. 3 serve solely for alignment purposes.

The chamber is filled via a gas cylinder containing 200 ppm of N_2O in pure nitrogen, while the working pressure is variable and is managed via a vacuum pump (PFEIFFER DualGauge), a pressure controller (PFEIFFER HiCUBE) and a system of needle valves (not shown in Fig. 3). In this way, it is possible to evaluate the acousto-optical response of the resonators–MEMS system for a constant concentration of the target gas and pressure.

The generated photo-acoustic signal is measured via Michelson interferometry [32]. A Helium-Neon (He-Ne) probe laser is split into two paths via a beam splitter (BS). One part is reflected and focused via a lens (CaF_2, f = 100 mm) and a wedged NBK-7 window on the high-reflectivity coated MEMS surface, while the transmitted part hits a mirror which acts as an immovable reference. The two back reflected beams are re-collected at the same BS, and finally sent to a photodetector. During the alignment phase, the reference arm is moved via a piezo driver connected to the WFG: this is done to simulate the continuous movement of the "racket-shaped" cantilever, thus optimally overlapping the two recombined beams. Four- and half-wave plates ($\lambda/2$ and $\lambda/4$ respectively, not shown in the figure) were used to maintain the same polarization state of the arms, thus maximizing the interferometric fringes. Finally, the photo-detector output signal is sent

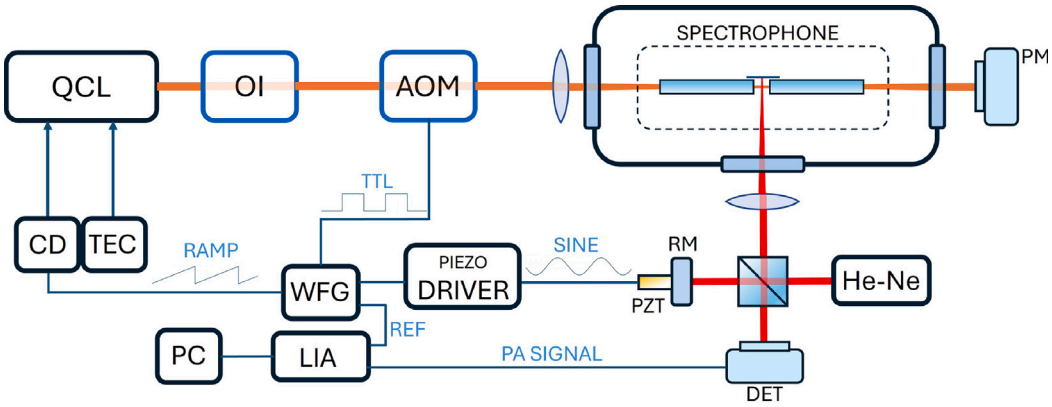

Fig. 3. Schematic representation of the setup. QCL: Quantum Cascade Laser. CD: current driver. TEC: temperature controller. OI: optical isolator. AOM: acousto-optical modulator. PM: power meter. He-Ne: Helium-Neon laser. RM: reference mirror. PZT: piezoelectric material DET: photo-detector. WFG: waveform generator. LIA: lock-in amplifier. REF: reference signal. For graphical reasons, the following components are not reported in the sketch: the gas pressure control system (a vacuum pump, a pressure controller, and a system of needle valves), and Four- and half-wave plates used to balance properly the interferometric arms.

to a lock-in amplifier (LIA, Zurich Instruments, 100 mHz 3 dB cut-off bandwidth), together with a TTL reference (REF) identical to the AOM input trigger, and the overall, R-component output is acquired at the trigger frequency, eliminating off-resonance signal components, and retrieving the 1f photo-acoustic (1f-PA) signal.

4. Result and discussion

4.1. Material comparison

During the material comparison, the pressure inside the chamber was fixed to 300 mbar. Each tube has been positioned at a distance of around 200 μm from the MEMS with the help of a USB microscope to avoid any contact. The acquired 1f-PA signals in the four cases have been compared to the spectra obtained with the "bare-MEMS" configuration (i.e. without any acoustic resonance) in the same working condition.

According to Fig. 4, compared to the signal obtained with the bare MEMS, whose peak value is equal to 10.86 mV, peak values equal to 102.88 mV, 97.63 mV, 103.71 mV, and 97.15 mV have been measured for stainless steel, brass, PLA and UV RESIN respectively, each of them corresponding to a peak signal enhancement equal to 9.47, 8.99, 9.55, and 8.95, as reported in the inset of Fig. 4. Discrepancies of less than 5% on the peak signal between the various materials investigated can be ascribed to slightly different positioning of the resonator tubes within the setup rather than to a difference in signal enhancement due to the material itself.

Furthermore, the surface roughness of the tubes due to manufacturing techniques does not bring appreciable differences to the phenomenon described, since the sound wavelength for a 7.18-kHz modulation corresponds to 47.8 mm, three orders of magnitude greater than the worst surface roughness analyzed (200 μm for PLA, see Fig. 2).

4.2. Best geometry investigation

Since the manufacturing material does not introduce appreciable differences in the amplification ability of the dual-tube system, the choice for the best geometry investigation fell on the UV Resin. In fact, if the subtractive techniques exploited for the metal tube fabrication are time-consuming and polluting, while the tubes made of PLA have very long production times (half an hour per pair), in the case of UV Resin it is possible to produce a high number of pairs of tube in a single one-hour processing.

In Fig. 5 an overview of the study is reported. To perform a comprehensive study, different sizes have been investigated in addition to the set described in Table 1, all designed to operate in the 7-kHz

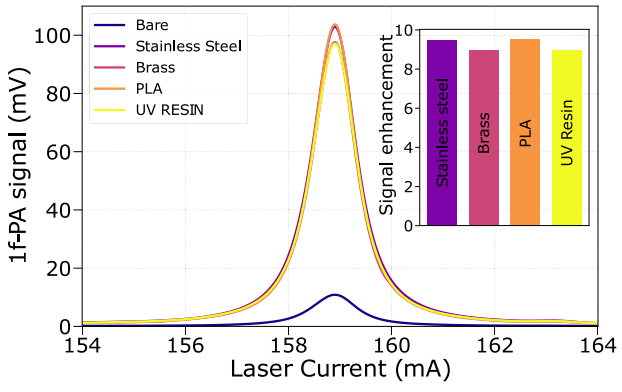

Fig. 4. Comparison between the 1f-PA spectra obtained with the dual-tube configurations of different materials (stainless steel in purple, brass in pink, PLA in orange, and UV RESIN in yellow) and the 1f-PA spectrum associated with the "bare-MEMS" configuration (depicted in blue). For all the traces the sample pressure within the aluminum cell is fixed at 300 mbar. **Inset**: signal enhancements with the four investigated material. These values are defined as the ratio between the peak signals in dual-tube and bare configurations.

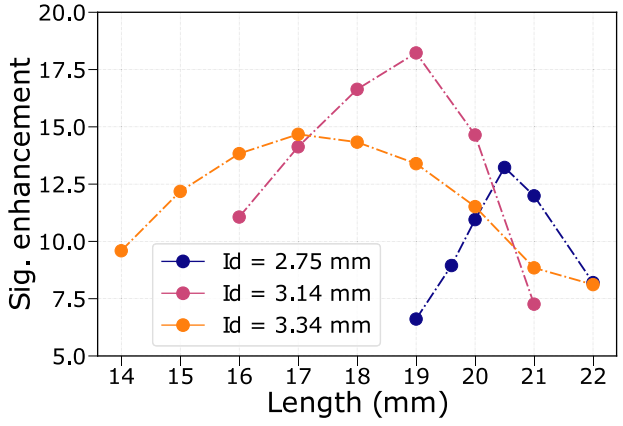

Fig. 5. Comparison between the signal enhancement of the dual-tube configuration made of UV Resin with different lengths and internal diameters. The three data sets are obtained fixing the internal diameter (purple trace I_D = 2.75 mm, pink trace I_D = 3.14 mm, and orange trace I_D = 3.34 mm respectively), and varying the single tube length.

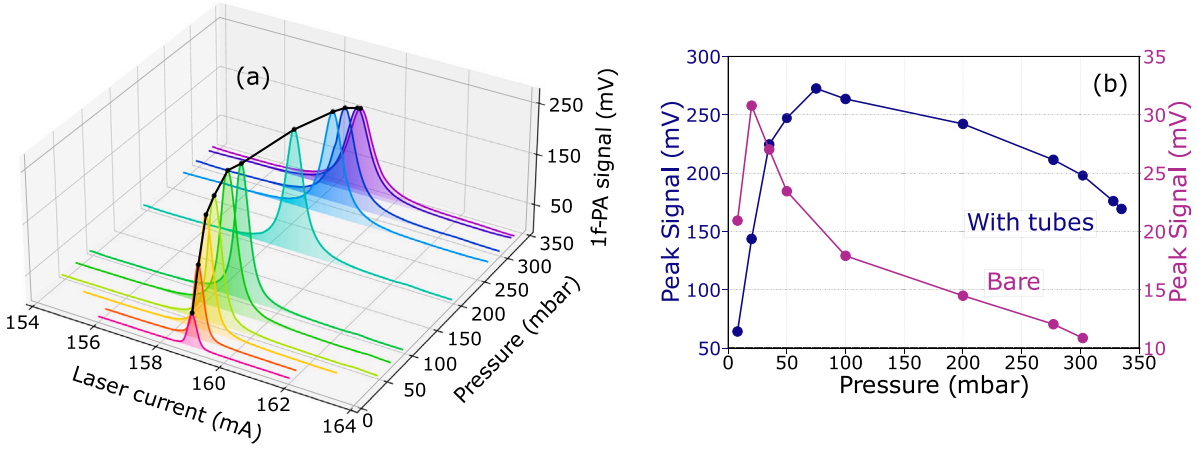

Fig. 6. **(a)**: 1f-PA spectra acquired with the best dual-tube configuration (I_D = 3.14 mm, L = 19 mm) as a function of the sample pressure. The black trace represents the envelope of the associated peak signal values. **(b)**: comparison of the peak signal values trends between the dual-tube (purple trace) and "bare-MEMS" (pink trace) configurations.

amplification range, as summarized in Fig. 5. For each pair of tubes, the 1f-PA spectra have been acquired, and the associated peak value has been compared with the one obtained in "bare-MEMS" configuration, retrieving the signal enhancement factor. These measurements have been performed in the same experimental condition of the material comparison.

Following the discussion made in Section 2, as the internal diameter of the resonators increases, the associated optimal length decreases. In fact, if for an internal diameter of 2.75 mm the associated optimal length is equal to 20.5 mm, when I_D is increased to 3.34 mm, L decreases up to 17 mm. The greatest signal enhancement, equal to 18.22, has been obtained with a pair of resonators with an internal diameter of 3.14 mm and a length of 19 mm. According to Eq. (1), the expected optimal resonator length with I_D = 3.14 mm and developed to amplify sound waves around 7.18 kHz should be 18.56 mm, highlighting that the experimental results are in good agreement with the theory.

4.3. System performance in the best configuration

The trend of the 1f-PA signal as a function of the pressure, ranging from 8 to 335 mbar, and obtained with the best dual-tube configuration (I_D = 3.14 mm, L = 19 mm), is reported in Fig. 6**(a)** together with the envelope of the peak values (black trace). Comparing this latter trend with the one associated to the "bare-MEMS" configuration (see Fig. 6**(b)**), it is evident that the coupling between the structure and the dual-tube determines a shift of the best working point at higher pressure.

In fact, if for the "bare-MEMS" configuration the highest peak signal, equal to 30.78 mV, has been measured at a pressure of 20 mbar, in the dual-tube configuration the best condition, associated with a peak signal equal to 272.52 mV, has been found at a pressure of 75 mbar. This evidence can be attributed to the acoustic enhancement pressure dependence, based on the necessity of having a suitable number of molecules for its maximization. Furthermore, following an increase of the signal in the low-pressure range, after reaching its maximum peak value, it explores a decrease at higher pressure due to the well-known increases of the pressure-depended viscous damping losses [45].

Then, for each value of pressure, a 60-second-long noise trace has been acquired with the same 3 dB cut-off LIA bandwidth used to collect the 1f-PA spectra (i.e. 100 mHz, corresponding to a LIA time constant equal to 0.8 s), and the standard deviation has been computed to retrieve the 1-σ noise. In this way it is easily possible to access both the signal-to-noise ratio (SNR) and the Noise Equivalent Concentration (NEC). The latter is defined as the ratio between the trace-gas concentration c (i.e. 200 ppm of N_2O) and the SNR. Both the trends of the SNR and the NEC as a function of the pressure are reported in Fig. 7.

The SNR remains approximately constant (ranging from 1.343×10^5 to 1.247×10^5), within 75 mbar and 300 mbar. The highest value, equal to 1.442×10^5, occurs at 200 mbar, where the photo-acoustic signal amplitude decrease due to the damping effect and the overall noise level reduction effects reaches an optimal trade-off, and a NEC of 1.39 part-per-billion is achieved.

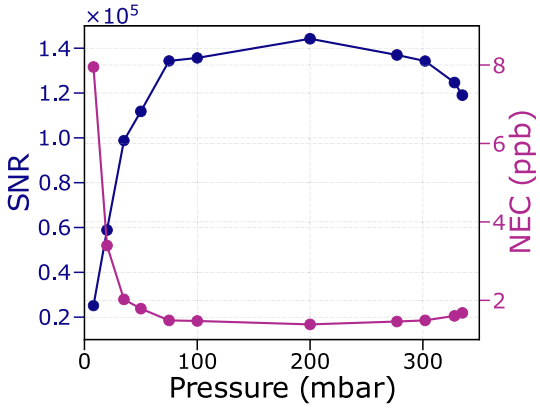

Fig. 7. SNR (purple trace), and MDL (pink trace) trends as a function of the sample pressure, both obtained setting the cut-off LIA bandwidth at 100 mHz.

Finally, the Allan–Werle deviation analysis has been performed to investigate the stability and the overall behavior of the spectrophone as a function of the integration time. The long-time noise trace has been acquired by fixing the laser current at the N_2O absorption peak but filling the chamber with 200 mbar of pure N_2 to prevent the interaction of the laser beam with any residual trace-gas spectral features. Furthermore, during the acquisition the 3B cut-off LIA bandwidth was set to 1 Hz, corresponding to an integration time of 0.08 s and a roll/off equal to 18 oct/decade. This choice allows the understanding of the sensor's performances in different time regimes, starting from its real-time response (i.e. at 0.08 s) up to an average response of 30 s, as shown in Fig. 8**(b)**.

At an integration time of 0.08 s (first point of the Allan–Werle deviation), the spectrophone achieves a NEC of 3.6 ppb, corresponding to a Normalize Noise Equivalent Absorption coefficient (NNEA) equal to 1.3×10^{-9} cm^{-1} W Hz$^{-1/2}$. Moving to 0.8 s, the NEC reaches a value in agreement with the one obtained from the 1-sigma noise analysis (equal to 1.3 ppb, represented by the red star in Fig. 8**(b)**), since they are both associated with the same integration time. Then, averaging up to 10 s allows the system to achieve a sub-ppb minimum detection limit,

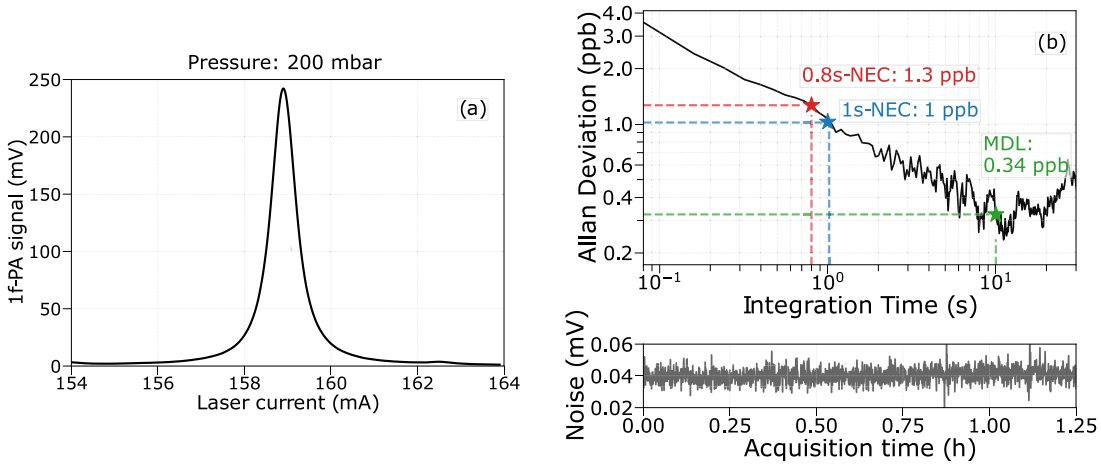

Fig. 8. (a): 1f-PA spectrum acquired at 200 mbar. **(b)**: long-time noise acquisition (bottom panel), and associated Allan deviation analysis (top panel) converted from noise level (mV) to noise equivalent concentration (ppb). The red star represents the point of the Allan deviation obtained at an integration time equal to 0.8 s, whose value is in accordance with the one estimated via the 1-σ analysis setting the LIA to 100 mHz of 3 dB cut-off LIA bandwidth (corresponding to a time constant of 0.8 s). The blue star represents the NEC obtained at 1 s of averaging time, while the green star is the MDL achieved when increasing the integration time up to 10 s.

Table 2
State-of-the-art single-pass photo-acoustic sensors for N_2O detection. The last row marked in bold identifies the results achieved in this work. To have a fair comparison, NEC values at the same integration time (1 s) have been reported, except for rows five and six. In these latter cases the 1 s-NEC values are neither declared in the main text, nor deducible from the graphs presented.

Year	Wavelength (μm)	Power (mW)	NNEA (cm^{-1} W $Hz^{-\frac{1}{2}}$)	NEC (ppb)	Integration time (s)
2013 [46]	4.61	400	2.9×10^{-9}	23	1
2014 [47]	7.83	250[b]	N.A.	6	1
2021 [48]	4.47	100	N.A.	20	1
2021 [49]	4.53	17.5[b]	5.69×10^{-9}	28	1
2022 [50]	4.52	25[b]	5.4×10^{-9}	7	0.1
2023 [51]	7.84	77	N.A.	9	0.1
2024 [52]	4.56	100	1.5×10^{-8}	4[b]	1
2024[a]	**4.56**	**15**	$\mathbf{1.3 \times 10^{-9}}$	**1**	**1**

N.A.: data not available.
[a] This work.
[b] Data extracted from the graphs of the related cited work.

being equal to 0.34 ppb (green star in Fig. 8**(b)**). Increasing further the integration time is no longer advantageous because the Allan deviation experiences an increase that worsens the overall performance at longer time scales

To conclude, considering the state-of-the-art of single-pass photo-acoustic sensors for this target molecule, summarized in detail in Table 2, our newly developed set-up emerges for several important advantages. Indeed, with an integration time comparable to previous literature (1 s), with an incident laser power as low as 15 mW, record values have been achieved for the NNEA coefficient (equal to 1.3×10^{-9}), and even better for the associated NEC (1 ppb), making this spectrophone ideal for further exploitation in more advanced configurations.

5. Conclusions

In this work, we have demonstrated how the combination of a high-performing "racket-shaped" silicon-based MEMS cantilever with an easy-to-build acoustic resonator, made by a dual-tube configuration, allows the development of a sub-ppb mid-IR trace-gas sensor addressing an N_2O fundamental roto-vibrational transition. As far as we know, this study reports a record value for single-pass PA-based N_2O trace gas sensing in terms of both Normalized Noise Equivalent Absorption coefficient and Noise Equivalent Concentration at 1 s integration time. Given the result achieved, future studies will be focused on parallel fronts. On one hand, due attention will be given to a further size reduction of the entire system, both testing new geometries and fabrication materials for the sample cell and developing alternative and more performing detection schemes to measure the photoacoustic signal. It is also worth mentioning that, as every photoacoustic sensor, even if the one developed in our work has been tested with N_2O, it can be in principle exploited for a broadband detection of a large variety of molecules exhibiting strong transitions in the mid-IR region. Finally, due to the relatively simple but effective design of the dual-tube configuration and the possibility of 3D-printing with a large variety of materials, a low-cost version of our set-up can be planned, with an easy integration with different MEMS classes. This will pave the way to the realization of mid-IR, high-performing gas sensors optimized for harsh environments and working conditions up to atmospheric pressure operations.

Abbreviations

The following abbreviations are used in this manuscript:

PAS	Photo-acoustic spectroscopy
MEMS	Micro-electro mechanical system
OEC	Open-end correction
ppb	Part-per-billion
MDL	Minimum detection limit
NNEA	Normalized noise equivalent absorption coefficient

CRediT authorship contribution statement

Stefano Dello Russo: Writing – review & editing, Writing – original draft, Software, Methodology, Investigation, Formal analysis, Data

curation. **Jacopo Pelini:** Writing – review & editing, Writing – original draft, Software, Methodology, Investigation, Formal analysis, Data curation. **Inaki Lopez Garcia:** Resources, Methodology. **Maria Concetta Canino:** Resources, Methodology, Conceptualization. **Alberto Roncaglia:** Resources, Methodology, Conceptualization. **Pablo Cancio Pastor:** Validation, Supervision, Methodology, Formal analysis. **Iacopo Galli:** Validation, Resources, Formal analysis, Conceptualization. **Paolo De Natale:** Supervision, Resources, Funding acquisition, Conceptualization. **Simone Borri:** Writing – review & editing, Validation, Supervision, Resources, Methodology, Investigation, Funding acquisition, Conceptualization. **Mario Siciliani de Cumis:** Writing – review & editing, Validation, Supervision, Resources, Methodology, Investigation, Funding acquisition, Conceptualization.

Declaration of competing interest

The authors declare the following financial interests/personal relationships which may be considered as potential competing interests: Paolo De Natale reports financial support was provided by European Defence Fund. Paolo De Natale reports financial support was provided by European Defence Agency. Paolo De Natale reports financial support was provided by Horizon Europe. Mario Siciliani de Cumis reports financial support was provided by MUR. Mario Siciliani de Cumis, Simone Borri, Inaki Lopez Garcia, Mariaconcetta Canico, Alberto Roncaglia, Pablo Cancio Pastor, Paolo De Natale has patent #WO2023126455A1 pending to Assignee. If there are other authors, they declare that they have no known competing financial interests or personal relationships that could have appeared to influence the work reported in this paper.

Data availability

Data will be made available on request.

Acknowledgments

Filippo Bonafè, Fabrizio Tamarri, Michele Sanmartin, Giulio Pizzochero, and Michele Bellettato are acknowledged for their contribution to the MEMS fabrication processing.

Funding

This work was partially supported by EDA under the Cat-B Project Q-LAMPS “Quantum LAser-based Multi-parametric Portable Sensor” (EDA contract n.B-PRJ-RT-989), by EU NextGenerationEU Programme with the I-PHOQS Infrastructure “Integrated infrastructure initiative in Photonic and Quantum Sciences” [IR0000016, ID D2B8D520], the QUANCOM project (MUR PON Ricerca e Innovazione 2014–2020 *ARS*0100734), the Laserlab-Europe Project [G.A. n. 871124], the MUQUABIS Project [G.A. n. 101070546] “Multiscale quantum bioimaging and spectroscopy”, by the European Union’s EDF Projects ADEQUADE “Advanced, Disruptive and Emerging QUAntum technologies for DEfense” (ID 101103417) and CASSATA “Covert and Advanced multi-modal Sensor Systems for tArget acquisition and reconnAissance” (ID 101121447).

References

[1] Jane Hodgkinson, Ralph P. Tatam, Optical gas sensing: a review, Meas. Sci. Technol. 24 (1) (2012) 012004.
[2] Armin Lambrecht, Katrin Schmitt, Mid-infrared gas-sensing systems and applications, in: Mid-Infrared Optoelectronics, Elsevier, 2020, pp. 661–715.
[3] Ravindra Kumar Jha, Non-dispersive infrared gas sensing technology: A review, IEEE Sens. J. 22 (1) (2021) 6–15.
[4] Ian Coddington, Nathan Newbury, William Swann, Dual-comb spectroscopy, Optica 3 (4) (2016) 414–426.
[5] G Giusfredi, I Galli, D Mazzotti, P Cancio, P De Natale, Theory of saturated-absorption cavity ring-down: radiocarbon dioxide detection, a case study, J. Opt. Soc. Am. B 32 (10) (2015) 2223–2237.
[6] G Giusfredi, S Bartalini, S Borri, P Cancio, Iacopo Galli, D Mazzotti, P De Natale, Saturated-absorption cavity ring-down spectroscopy, Phys. Rev. Lett. 104 (11) (2010) 110801.
[7] Sandrine Galtier, Clément Pivard, Patrick Rairoux, Towards DCS in the UV spectral range for remote sensing of atmospheric trace gases, Remote Sens. 12 (20) (2020) 3444.
[8] Alexander Gurlo, Ralf Riedel, In situ and operando spectroscopy for assessing mechanisms of gas sensing, Angew. Chem. Int. Ed. 46 (21) (2007) 3826–3848.
[9] Lei Xu, Zhengfei Dai, Guotao Duan, Lianfeng Guo, Yi Wang, Hong Zhou, Yanxiang Liu, Weiping Cai, Yuelin Wang, Tie Li, Micro/nano gas sensors: A new strategy towards in-situ wafer-level fabrication of high-performance gas sensing chips, Sci. Rep. 5 (1) (2015) 1–12.
[10] Aditya Sharma, Chandra Sekhar Rout, Advances in understanding the gas sensing mechanisms by in situ and operando spectroscopy, J. Mater. Chem. A 9 (34) (2021) 18175–18207.
[11] Christoph Haisch, Photoacoustic spectroscopy for analytical measurements, Meas. Sci. Technol. 23 (1) (2011) 012001.
[12] Stefan Palzer, Photoacoustic-based gas sensing: A review, Sensors 20 (9) (2020) 2745.
[13] Fupeng Wang, Yaopeng Cheng, Qingsheng Xue, Qiang Wang, Rui Liang, Jinghua Wu, Jiachen Sun, Cunguang Zhu, Qian Li, Techniques to enhance the photoacoustic signal for trace gas sensing: A review, Sensors Actuators A 345 (2022) 113807.
[14] Alaa Fathy, Yasser M Sabry, Ian W Hunter, Diaa Khalil, Tarik Bourouina, Direct absorption and photoacoustic spectroscopy for gas sensing and analysis: a critical review, Laser Photonics Rev. 16 (8) (2022) 2100556.
[15] Xinyu Zhao, HongChao Qi, Yufu Xu, Chenxi Li, Min Guo, Ke Chen, Fiber-optic photoacoustic gas sensing: a review, Appl. Spectrosc. Rev. (2024) 1–29.
[16] Chenxi Li, Xiao Han, Min Guo, Hongchao Qi, Heng Wang, Xinyu Zhao, Ke Chen, Fiber-optic photoacoustic gas microsensor dual enhanced by Helmholtz resonator and interferometric cantilever, Anal. Chem. (2024).
[17] Allan Rosencwaig, Photoacoustic spectroscopy, Annu. Rev. Biophys. Bioeng. 9 (1) (1980) 31–54.
[18] Gary A West, Joseph J Barrett, Donald R Siebert, K Virupaksha Reddy, Photoacoustic spectroscopy, Rev. Sci. Instrum. 54 (7) (1983) 797–817.
[19] Anatoliy A Kosterev, Yu A Bakhirkin, Robert F Curl, Frank K Tittel, Quartz-enhanced photoacoustic spectroscopy, Opt. Lett. 27 (21) (2002) 1902–1904.
[20] Pietro Patimisco, Gaetano Scamarcio, Frank K Tittel, Vincenzo Spagnolo, Quartz-enhanced photoacoustic spectroscopy: a review, Sensors 14 (4) (2014) 6165–6206.
[21] Klaus Wilcken, Jyrki Kauppinen, Optimization of a microphone for photoacoustic spectroscopy, Appl. Spectrosc. 57 (9) (2003) 1087–1092.
[22] Yonggang Yin, Danyang Ren, Chiye Li, Ruimin Chen, Junhui Shi, Cantilever-enhanced photoacoustic spectroscopy for gas sensing: A comparison of different displacement detection methods, Photoacoustics 28 (2022) 100423.
[23] Sheng Zhou, Martin Slaman, Davide Iannuzzi, Demonstration of a highly sensitive photoacoustic spectrometer based on a miniaturized all-optical detecting sensor, Opt. Express 25 (15) (2017) 17541–17548.
[24] Zhengyuan Zhang, Xinhong Fan, Yufu Xu, Yongqi Wang, Yiyao Tang, Rui Zhao, Chenxi Li, Heng Wang, Ke Chen, Silicon-cantilever-enhanced single-fiber photoacoustic acetylene gas sensor, Sensors 23 (17) (2023) 7644.
[25] Maxime Duquesnoy, Guillaume Aoust, Jean-Michel Melkonian, Raphaël Lévy, Myriam Raybaut, Antoine Godard, Quartz enhanced photoacoustic spectroscopy based on a custom quartz tuning fork, Sensors 19 (6) (2019) 1362.
[26] Pietro Patimisco, Angelo Sampaolo, Marilena Giglio, Stefano Dello Russo, Verena Mackowiak, Hubert Rossmadl, Alex Cable, Frank K Tittel, Vincenzo Spagnolo, Tuning forks with optimized geometries for quartz-enhanced photoacoustic spectroscopy, Opt. Express 27 (2) (2019) 1401–1415.
[27] Shunda Qiao, Ying He, Haiyue Sun, Pietro Patimisco, Angelo Sampaolo, Vincenzo Spagnolo, Yufei Ma, Ultra-highly sensitive dual gases detection based on photoacoustic spectroscopy by exploiting a long-wave, high-power, wide-tunable, single-longitudinal-mode solid-state laser, Light: Sci. Appl. 13 (1) (2024) 100.
[28] Yahui Liu, Shunda Qiao, Chao Fang, Ying He, Haiyue Sun, Jian Liu, Yufei Ma, A highly sensitive LITES sensor based on a multi-pass cell with dense spot pattern and a novel quartz tuning fork with low frequency, Opto-Electron. Adv. 7 (3) (2024) 230230.
[29] Adv Van der Ziel, Flicker noise in electronic devices, in: Advances in Electronics and Electron Physics, Vol. 49, Elsevier, 1979, pp. 225–297.
[30] Friits N. Hooge, 1/f noise sources, IEEE Trans. Electron Dev. 41 (11) (1994) 1926–1935.
[31] Jacopo Pelini, Stefano Dello Russo, Inaki Lopez Garcia, Maria Concetta Canino, Alberto Roncaglia, Pablo Cancio Pastor, Iacopo Galli, Wei Ren, Paolo De Natale, Zhen Wang, Simone Borri, Mario Siciliani de Cumis, New silicon-based micro-electro-mechanical systems for photo-acoustic trace-gas detection, Photoacoustics (2024) 100619.

[32] Mario Siciliani de Cumis, Simone Borri, Mariaconcetta Canino, Pablo Cancio Pastor, Paolo De Natale, Inaki Lopez Garcia, Alberto Roncaglia, Photoacoustic spectroscopy sensor for trace gas detection and method for trace gas detection, Pat. Pending WO2023126455A1.

[33] A Borrielli, Antonio Pontin, Francesco Saverio Cataliotti, Lorenzo Marconi, Francesco Marin, F Marino, G Pandraud, GA Prodi, E Serra, M Bonaldi, Low-loss optomechanical oscillator for quantum-optics experiments, Phys. Rev. Appl. 3 (5) (2015) 054009.

[34] Jingsong Li, Weidong Chen, Benli Yu, Recent progress on infrared photoacoustic spectroscopy techniques, Appl. Spectrosc. Rev. 46 (6) (2011) 440–471.

[35] Stefano Dello Russo, Marilena Giglio, Angelo Sampaolo, Pietro Patimisco, Giansergio Menduni, Hongpeng Wu, Lei Dong, Vittorio MN Passaro, Vincenzo Spagnolo, Acoustic coupling between resonator tubes in quartz-enhanced photoacoustic spectrophones employing a large prong spacing tuning fork, Sensors 19 (19) (2019) 4109.

[36] Guillaume Aoust, Raphael Levy, Myriam Raybaut, Antoine Godard, Jean-Michel Melkonian, Michel Lefebvre, Theoretical analysis of a resonant quartz-enhanced photoacoustic spectroscopy sensor, Appl. Phys. B 123 (2017) 1–11.

[37] Huadan Zheng, Lei Dong, Angelo Sampaolo, Hongpeng Wu, Pietro Patimisco, Xukun Yin, Weiguang Ma, Lei Zhang, Wangbao Yin, Vincenzo Spagnolo, et al., Single-tube on-beam quartz-enhanced photoacoustic spectroscopy, Opt. Lett. 41 (5) (2016) 978–981.

[38] Ke Chen, Hong Deng, Min Guo, Chen Luo, Shuai Liu, Bo Zhang, Fengxiang Ma, Feng Zhu, Zhenfeng Gong, Wei Peng, et al., Tube-cantilever double resonance enhanced fiber-optic photoacoustic spectrometer, Opt. Laser Technol. 123 (2020) 105894.

[39] Qian Wu, Haohua Lv, Leqing Lin, Hongpeng Wu, Marilena Giglio, Wenguo Zhu, Yongchun Zhong, Angelo Sampaolo, Pietro Patimisco, Lei Dong, et al., Clamp-type quartz tuning fork enhanced photoacoustic spectroscopy, Opt. Lett. 47 (17) (2022) 4556–4559.

[40] Stefano Dello Russo, Sheng Zhou, Andrea Zifarelli, Pietro Patimisco, Angelo Sampaolo, Marilena Giglio, Davide Iannuzzi, Vincenzo Spagnolo, Photoacoustic spectroscopy for gas sensing: A comparison between piezoelectric and interferometric readout in custom quartz tuning forks, Photoacoustics 17 (2020) 100155.

[41] Xinyu Zhao, Chenxi Li, Hongchao Qi, Jiayu Huang, Yufu Xu, Zhengzhi Wang, Xiao Han, Min Guo, Ke Chen, Integrated near-infrared fiber-optic photoacoustic sensing demodulator for ultra-high sensitivity gas detection, Photoacoustics 33 (2023) 100560.

[42] Naohisa Ogawa, Fumitoshi Kaneko, Open end correction for a flanged circular tube using the diffusion process, Eur. J. Phys. 34 (5) (2013) 1159.

[43] Harold Levine, Julian Schwinger, On the radiation of sound from an unflanged circular pipe, Phys. Rev. 73 (4) (1948) 383.

[44] Pietro Patimisco, Angelo Sampaolo, Yves Bidaux, Alfredo Bismuto, Marshall Scott, James Jiang, Antoine Muller, Jerome Faist, Frank K Tittel, Vincenzo Spagnolo, Purely wavelength-and amplitude-modulated quartz-enhanced photoacoustic spectroscopy, Opt. Express 24 (23) (2016) 25943–25954.

[45] Pietro Patimisco, Angelo Sampaolo, Verena Mackowiak, Hubert Rossmadl, Alex Cable, Frank K Tittel, Vincenzo Spagnolo, Loss mechanisms determining the quality factors in quartz tuning forks vibrating at the fundamental and first overtone modes, IEEE Trans. Ultrason. Ferroelectr. Freq. Control 65 (10) (2018) 1951–1957.

[46] Yufei Ma, Rafał Lewicki, Manijeh Razeghi, Frank K Tittel, QEPAS based ppb-level detection of CO and N 2 O using a high power CW DFB-QCL, Opt. Express 21 (1) (2013) 1008–1019.

[47] Mohammad Jahjah, Wei Ren, Przemysław Stefański, Rafał Lewicki, Jiawei Zhang, Wenzhe Jiang, Jan Tarka, Frank K Tittel, A compact QCL based methane and nitrous oxide sensor for environmental and medical applications, Analyst 139 (9) (2014) 2065–2069.

[48] Ismail Bayrakli, A portable N2O sensor based on quartz-enhanced photoacoustic spectroscopy with a distributed-feedback quantum cascade laser for medical and atmospheric applications, Opt. Quantum Electron. 53 (11) (2021) 642.

[49] Yuan Cao, Ruifeng Wang, Jie Peng, Kun Liu, Weidong Chen, Guishi Wang, Xiaoming Gao, Humidity enhanced N2O photoacoustic sensor with a 4.53 μm quantum cascade laser and Kalman filter, Photoacoustics 24 (2021) 100303.

[50] Andrea Zifarelli, Raffaele De Palo, Pietro Patimisco, Marilena Giglio, Angelo Sampaolo, Stéphane Blaser, Jérémy Butet, Olivier Landry, Antoine Müller, Vincenzo Spagnolo, Multi-gas quartz-enhanced photoacoustic sensor for environmental monitoring exploiting a vernier effect-based quantum cascade laser, Photoacoustics 28 (2022) 100401.

[51] Giansergio Menduni, Andrea Zifarelli, Elena Kniazeva, Stefano Dello Russo, Ada Cristina Ranieri, Ezio Ranieri, Pietro Patimisco, Angelo Sampaolo, Marilena Giglio, Fabrizio Manassero, et al., Measurement of methane, nitrous oxide and ammonia in atmosphere with a compact quartz-enhanced photoacoustic sensor, Sensors Actuators B 375 (2023) 132953.

[52] Min Yang, Zhen Wang, Haojia Sun, Mengyuan Hu, Pak To Yeung, Qinxue Nie, Shanliang Liu, Naota Akikusa, Wei Ren, Highly sensitive QEPAS sensor for sub-ppb N2O detection using a compact butterfly-packaged quantum cascade laser, Appl. Phys. B 130 (1) (2024) 6.

Stefano Dello Russo obtained his M.S. degree (cum laude) in Physics in 2018 from the University of Bari. From the same year, he is a Ph.D. student at the Physics Department of the University of Bari, developing his research work at PolySense Lab, joint-research laboratory between Technical University of Bari and THORLABS GmbH. Currently, he is working as a researcher at the Italian Space Agency (ASI). His research activity is focused on Spectroscopy, Metrology and Quantum Communications.

Jacopo Pelini obtained his Master's Degree in Physics in 2021 from the University of Perugia. Currently, he is a Ph.D. student in Quantum Technologies at the University "Federico II" of Naples, and CNR-INO in Florence. His research focuses on Cantilever-Enhanced photo-acoustic spectroscopy, Micro-Electro-Mechanical Systems characterization, and frequency stabilization of semiconductor mid-infrared laser sources.

Iñaki Lopez Garcia received his Ph.D. in Physic from Complutense University of Madrid (Spain) in 2014. He has worked, and collaborated for several institutes at Italian research council (CNR). His research interests include nanophysics, gas sensing, nonlinear optics, electron microscopy and phase change memories. His work has been published in several peer-reviewed journals.

Marica Canino, Ph.D. in Physics since 2007, joined the Institute for Microelectronics and Microsystems of CNR in 2008. Since 2018 she is permanent staff. In her research, she studies the physics of the fabrication processes of silicon-based and silicon carbide-based microelectronic devices and advanced solar cells with special focus on material doping.

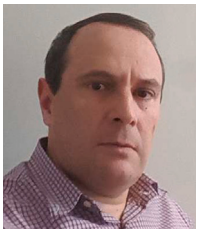

Alberto Roncaglia received a M. Sc. Degree (cum laude) in Electrical Engineering and a Ph. D. degree in Electronics and Computer Science in 1998 and 2002, respectively, both from the University of Bologna. In 2001 he joined the Institute of Microelectronics and Microsystems (IMM) of the Italian National Research Council (CNR) as a scientific researcher. He has been involved in several EUfunded projects, such as Underground M3 (Eurocores ESF Programme), ROBOSPECT (FP7-ICTRobotics), SiNERGY (FP7-NMP), AEROBI (H2020-ICT-Robotics), Q-SORT (H2020-FETOPEN), RESIST (H2020-MG), SiC Nano for PicoGeo (H2020-FETOPEN), 5D NanoPrinting (H2020FETOPEN), MOLIERE (EIT Manufacturing 2022). His research interests include design, simulation and technology development for the fabrication of micro- and nano-electro-mechanical systems (MEMS and NEMS).

Pablo Cancio Pastor received the Graduate degree in physics from Complutense University of Madrid in 1986, and the Ph.D. degree in physics from the Autonoma University of Madrid in 1992. At present, he is a permanent Staff Researcher of the National Institute of Optics, Italian National Research Council, Florence (CNR-INO). He is an expert in state-of-the-art laser sources in the visible-infrared spectral regions including optical frequency combs, nonlinear optical generated coherent sources, semiconductor diode lasers and quantum-cascade lasers. His current research interests include high-precision and high-sensitivity atomic and molecular spectroscopy by using high-resolution laser spectrometers.

Iacopo Galli was born in Firenze (Italy), in 1976. He received the Laurea degree in physics. In 2004 and the Ph.D. degree in physics in 2009 from the University of Florence. Since 2004 he works for INO-CNR:

2012 - Research scientist at the Italian National Research Council - Institute of Optics (CNR-INO).

2023 - Senior research scientist at the Italian National Research Council - Institute of Optics (CNRINO).

2016 - Cofounder of ppqSense S.r.l.

His main research interests include nonlinear optics, high-sensitivity and high-precision infrared spectroscopy, frequency metrology, and quantum cascade lasers.

Paolo De Natale is research director at the National Institute of Optics-INO (Italian CNR) and member of the Directive Council of LENS, Firenze, Italy. In the years 2007–2021 was director of the National Institute of Optics of the Italian National Research Council (INO-CNR, former INOA). He is the Italian representative in the Quantum Community Network (QCN) Board of the EU Flagship on Quantum Technologies and in the Optronics CapTech of the European Defense Agency-EDA. Scientific interests include photonics, atomic and molecular physics, nonlinear optics and quantum technologies. He is author of more than 360 publications, owns 9 patents and is a cofounder of two former CNR spin-off companies, ppqSense srl and QTI srl. He is Fellow of IEEE (since 2011) and OSA (since 2015).

Simone Borri completed his Ph.D. in 2007 from the University of Firenze, Italy. He has been a researcher at CNR-National Institute of Optics since 2010. He worked as a researcher for LENS, the European Laboratory for Nonlinear Spectroscopy, and IFN, the Italian Institute for Photonics and Nanotechnologies. His main expertise is in the development of coherent sources and techniques for high-sensitivity and high-resolution molecular spectroscopy in the mid-infrared. After demonstrating the first cavity-enhanced QEPAS system, he is now working on high-performing CEPAS sensors combining mid-infrared lasers, custom-made cantilevers, and high-finesse resonant cavities.

Mario Siciliani de Cumis, Ph.D. in Physics at University of Catania and LENS. He was postdoctoral researcher at CNR in Florence from 2009 to 2015 and temporary researcher at INRIM in Turin until 2016. From 2017 he is permanent researcher at ASI in Matera. His activities concern experiments about Nonlinear Optics, Spectroscopy, Sensors, Metrology, Laser and Quantum Technologies. He is author of a patent on Photoacoustics sensors and about 50 papers on peer-reviewed journals collecting over 1000 citations.